

## Article

# Effects of Zr Content on the Microstructure and Performance of TiMoNbZr<sub>x</sub> High-Entropy Alloys

Gengbiao Chen <sup>1</sup>, Yi Xiao <sup>1</sup>, Xixi Ji <sup>1</sup>, Xiubing Liang <sup>2</sup>, Yongle Hu <sup>1</sup> , Zhihai Cai <sup>3</sup>, Jian Liu <sup>3</sup> and Yonggang Tong <sup>1,\*</sup>

<sup>1</sup> College of Automobile and Mechanical Engineering, Changsha University of Science and Technology, Changsha 410114, China; 006529@csust.edu.cn (G.C.); 19103010463@stu.csust.edu.cn (Y.X.); jixixi201408@163.com (X.J.); yonglehu@126.com (Y.H.)

<sup>2</sup> National Institute of Defense Technology Innovation, Academy of Military Sciences PLA China, Beijing 100072, China; liangxb\_d@163.com

<sup>3</sup> National Key Laboratory for Remanufacturing, Army Academy of Armored Forces, Beijing 100072, China; caizhihai2052@163.com (Z.C.); baiduxiao@hotmail.com (J.L.)

\* Correspondence: tongyonggang\_csust@163.com

**Abstract:** TiMoNbZr<sub>x</sub> refractory high-entropy alloys were prepared by vacuum arc melting, and the influence of the Zr alloying element and its content on the phases, microstructure, mechanical properties, and wear resistance of TiMoNbZr<sub>x</sub> alloys was explored. It was found that the alloys after Zr addition were composed of a single BCC phase. Upon increasing the Zr content, the grain size of the as-cast alloy decreased first and then increased, and TiMoNbZr<sub>0.5</sub> exhibited the smallest grain size. Adding an appropriate amount of Zr increased the strength and hardness of the alloys. TiMoNbZr<sub>0.5</sub> exhibited the best wear resistance, with a friction coefficient of about 0.33. It also displayed the widest wear scar, the shallowest depth, and the greatest degree of wear on the grinding ball because of the formation of an oxide film during wear.

**Keywords:** high-entropy alloy; microstructure; mechanical properties; processing



**Citation:** Chen, G.; Xiao, Y.; Ji, X.; Liang, X.; Hu, Y.; Cai, Z.; Liu, J.; Tong, Y. Effects of Zr Content on the Microstructure and Performance of TiMoNbZr<sub>x</sub> High-Entropy Alloys. *Metals* **2021**, *11*, 1315. <https://doi.org/10.3390/met11081315>

Academic Editors: Oleg N. Senkov, Panagiotis (Panos) Tsakiroopoulos, Jean-Philippe Couzinie and Jiro Kitagawa

Received: 29 June 2021

Accepted: 16 August 2021

Published: 19 August 2021

**Publisher's Note:** MDPI stays neutral with regard to jurisdictional claims in published maps and institutional affiliations.



**Copyright:** © 2021 by the authors. Licensee MDPI, Basel, Switzerland. This article is an open access article distributed under the terms and conditions of the Creative Commons Attribution (CC BY) license (<https://creativecommons.org/licenses/by/4.0/>).

## 1. Introduction

Refractory high-entropy alloys were first proposed in 2010 [1] as promising candidates for use in high-temperature components of aerospace engines and turbine blades due to their excellent mechanical performance, thermal stability, corrosion resistance, and oxidation resistance [2–11]. Refractory high-entropy alloys are mainly composed of high-melting-point elements of the IV, V, and VI subgroups. The properties of such alloys can be improved by adding elements or adjusting the ratio of elements. Reported refractory high-entropy alloys include NbTaMoW [12–15], TaNbHfZrTi [16–19], NbMoTaWV [20–22], NbTiVZr [23–26], and AlNbTiZrTa<sub>0.5</sub>Mo<sub>0.5</sub> [27–29]. Due to their extraordinary thermal resistance, studies of refractory high-entropy alloys have focused on their mechanical performance [30–34], while few studies have investigated their wear resistance [35]. Pouliat et al. [36,37] used vacuum arc melting to prepare MoTaWNbV and MoTaNbZrTi alloys and studied their wear resistance under different conditions. It was found that the wear resistance of MoTaNbZrTi was better than MoTaWNbV, followed by Inconel 718 superalloy. MoTaNbZrTi contained Ti, Zr, and other easily oxidizable elements, resulting in the generation of oxides on the contact surface, which played a lubricating effect that helped reduce the wear of the alloy; however, MoTaWNbV and MoTaNbZrTi had low plasticities of 2.3% and 3%, respectively, which hindered their engineering applications. Recently, Zhu et al. [38] used mechanical alloying and spark plasma sintering to prepare TiMoNb alloys and found that the cast TiMoNb alloy had a microstructure composed of the BCC phase. The interface structure and chemical structure of the TiMoNb alloy were adjusted to form high-density Ti-rich nanoscale precipitates that displayed high thermal stability and wear resistance, the latter of which was comparable to alumina at room temperature. At 600 °C, the TiMoNb alloy still showed a very low wear

rate ( $\sim 10^{-6} \text{ mm}^3/(\text{N m})$ ), but its hardness and strength were relatively low, making it unsuitable for applications as a wear-resistant material.

Improving the plasticity of this alloy while ensuring its excellent wear resistance may further expand the development of other refractory high-entropy alloys for friction and wear-resistant materials. Zeng et al. [39] confirmed that Al and Cr atoms were prone to oxidation and formed  $\text{Cr}_2\text{O}_3$  and  $\text{Al}_2\text{O}_3$  layers. The oxidation products produced by the coating played an important role in the formation of a lubricating film and exhibited good wear resistance. In addition, it was found that the presence of Zr generated oxides on the wear surface of the alloy, which provided a lubricating effect and improved the wear resistance of the alloy [37]. In addition, Tong et al. [40] studied the effect of alloying elements (Cr, Zr, V, Hf, and Re) on the strength-plasticity trade-off of NbMoTaW refractory high-entropy alloys. Through first-principles calculations and experiments, they found that the addition of Zr simultaneously improved the ductility and strength of the alloy. In other investigations, Mo, Cr, Nb, Ti, V, and other elements also improved the strength-plasticity trade-off of such alloys [41–45].

Based on the above considerations, in this paper, Zr was added to TiMoNb alloy to strengthen it and improve its wear resistance. TiMoNbZr<sub>x</sub> high-entropy alloys ( $x = 0, 0.5, 1, x =$  the molar ratio, hereinafter referred to as Zr<sub>0</sub>, Zr<sub>0.5</sub>, Zr<sub>1</sub>) were prepared by vacuum arc melting. The effect of the Zr content on the microstructure, mechanical properties, and wear resistance of the TiMoNb high-entropy alloys was studied.

## 2. Experimental Methods

The raw materials included high-purity (>99.99%) metal blocks (Ti, Mo, Nb, and Zr). Button-shaped TiMoNbZr<sub>x</sub> refractory high-entropy alloy ingots were prepared by arc melting. Each ingot was smelted at least five times under the protection of pure Ar gas to ensure the uniformity of the alloy components. DK77 wire EDM was used to cut, polish, clean, and dry samples for later use. X-ray diffractometry (XRD, Cu K $\alpha$  radiation, Rigaku D/Max 2550VB, BRUKER, Billerica, MA, USA) was used to analyze the phases in the alloy, with a scanning speed of 5°/min and a scanning range of 20–80°. Scanning electron microscopy (SEM) (Phenom, Eindhoven, The Netherlands) was used to characterize the microstructure, and energy-dispersive spectrometry (EDS) (Phenom, Eindhoven, The Netherlands) was used for element composition analysis.

An HVST-1000Z semi-automatic Vickers hardness tester (Laizhou Wei Yi Test Equipment Manufacturing Co, Shandong, China) was used to test the hardness of the alloy (static load: 100 g; holding time: 15 s). In total, 10 data points were collected for each sample, and the average value was taken. Samples with a size of  $\Phi 5 \text{ mm} \times 8 \text{ mm}$  were cut from the ingots, and a CMT5105GL electronic universal tensile testing machine (SUST, Zhuhai, China) was used to test the compressive mechanical properties at room temperature with a loading rate of 0.5 mm/min. The ingots were cut into block specimens with dimensions of 20 mm  $\times$  15 mm  $\times$  4 mm. The samples were polished with SiC water-abrasive sandpaper, and the anti-friction and wear properties of the alloys were tested by MDW-05 reciprocating friction and wear tester (Jinan Yihua Tribology Testing Technology Co., Ltd., Jinan, China). The grinding ball was Si<sub>3</sub>N<sub>4</sub> with a size of  $\Phi 6 \text{ mm}$ . The loads were 30, 50, and 100 N, the running time was 30 min, and the frequency was 2 Hz. Dry sliding wear tests were carried out at room temperature in a nonlubricated manner. The samples were ultrasonically cleaned with acetone before and after wear, and the width and depth of the wear scar were measured using a two-dimensional profiler to analyze the wear resistance of the alloy.

## 3. Results and Discussion

### 3.1. Phase Structure

Figure 1 shows the XRD pattern of (a) the TiMoNbZr<sub>x</sub> high-entropy alloy and (b) an enlarged view of the main diffraction peak. It can be seen from Figure 1a that the alloys after Zr addition were composed of a single BCC phase. As shown in Figure 1b, upon increasing the Zr content, the main diffraction peak of the BCC phase shifted to a lower

diffraction angle, and the lattice constant of the alloy increased, with lattice parameters of 3.26 Å, 3.28 Å, and 3.29 Å for  $Zr_0$ ,  $Zr_{0.5}$ , and  $Zr_1$ , respectively. The atomic sizes of Ti, Mo, and Nb are 1.47, 1.47, and 1.4, respectively, which are similar, while Zr has an atomic size of 1.6, which is much larger than that of Ti, Mo, and Nb; thus, the lattice distortion of the alloy increased upon increasing the Zr content.

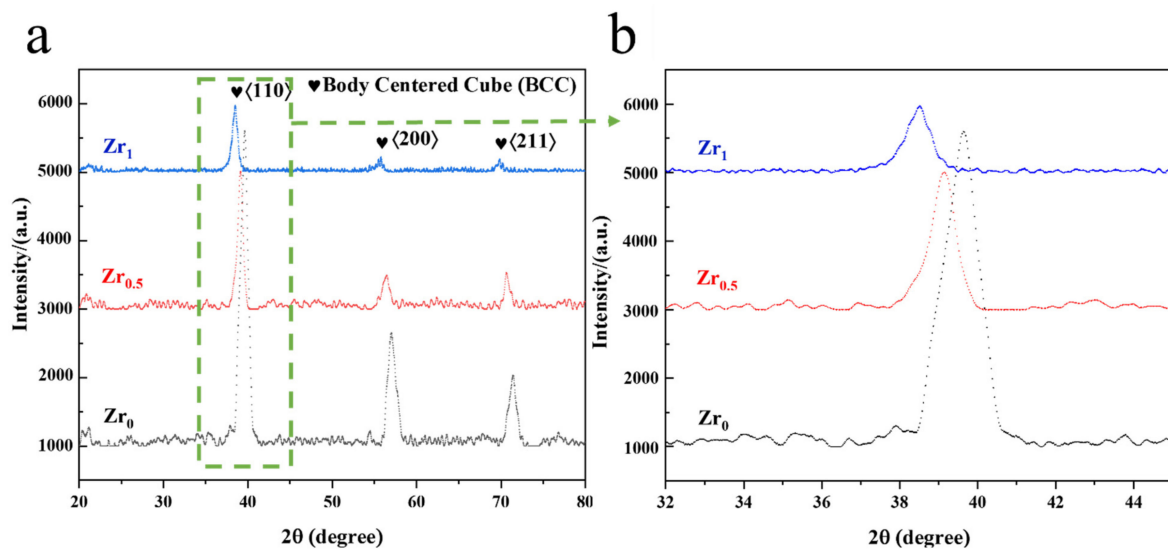


**Figure 1.** (a) XRD patterns of the  $TiMoNbZr_x$  HEAs; (b) magnified main diffraction peak of the  $TiMoNbZr_x$  HEAs.

### 3.2. Microstructure

SEM was used to characterize the microstructure of the  $TiMoNbZr_x$  high-entropy alloys. The SEM image and EDS analysis of the alloy are shown in Figure 2 and Table 1. Figure 2a shows that the structure of the  $Zr_0$  alloy is a typical equiaxed crystal, with an average grain size of 200  $\mu m$ . In addition, some black precipitates (volume fraction of approx. 0.42% by ImageJ software) appeared in the grains, which is known to be a Ti-rich precipitate according to Ref. [38].  $Zr_{0.5}$  alloy displayed a dendritic morphology, with disordered grains with a size range of 40–80  $\mu m$  (Figure 2b). It can be observed from Figure 2c that the  $Zr_1$  alloy has an equiaxed crystal morphology, with an average grain size of 120  $\mu m$ . This shows that the dendritic morphology of the as-cast alloy was quite different from that of alloys with different Zr contents. Upon increasing the Zr content, the alloy grain size first decreased and then increased.

**Table 1.** Nominal and actual compositions of the  $TiMoNbZr_x$  HEAs.

Alloy	Ingredient	Region	Element Content/at %			
			Ti	Mo	Nb	Zr
$Zr_0$	Nominal		33.33	33.33	33.33	-
	Actual	GB	35.28	32.24	32.48	-
		IG	31.26	33.95	34.79	-
$Zr_{0.5}$	Nominal		28.57	28.57	28.57	14.29
	Actual	ID	31.23	24.27	27.96	16.54
		DR	26.18	31.88	28.96	12.98
$Zr_1$	Nominal		25.00	25.00	25.00	25.00
	Actual	GB	28.32	19.18	24.66	27.84
		IG	23.27	29.84	25.63	21.26

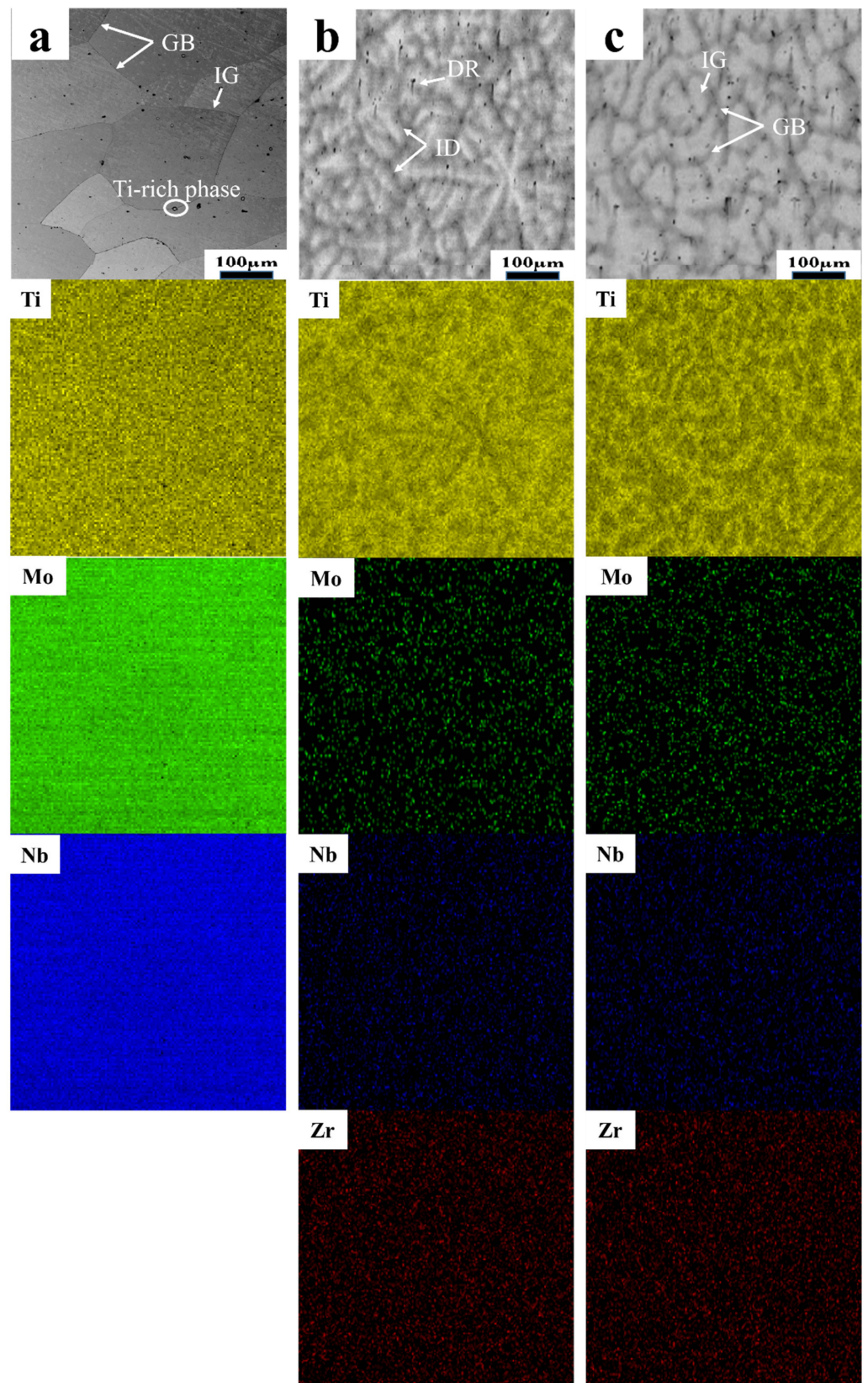


**Figure 2.** SEM and EDS images of the TiMoNbZr<sub>x</sub> HEAs: (a) Zr<sub>0</sub>; (b) Zr<sub>0.5</sub>; (c) Zr<sub>1</sub>.

According to the SEM images and EDS results, element segregation occurred in the Zr<sub>0</sub> alloy, in which Ti atoms accumulated in the interior of the grain (IG) region, while Mo and Nb atoms were uniformly distributed throughout the alloy. In the Zr<sub>0.5</sub> alloy structure,

Nb was evenly distributed, while Ti and Zr were mainly distributed between dendrites (DR), and Mo was mainly distributed in the dendritic arm (ID). In the  $Zr_1$  alloy structure, Nb was relatively uniformly distributed, Ti and Zr were mainly distributed between GB, and Mo was mainly distributed in the IG.

### 3.3. Mechanical Performance

To explore the influence of alloying element Zr on the mechanical performance of the alloy, room-temperature compression mechanical performance tests were carried out. The stress–strain curves in Figure 3 show that the yield strength of the  $Zr_0$  alloy was  $1109 \pm 28$  MPa, its compressive strength was  $1416 \pm 14$  MPa, and its plasticity was  $12 \pm 1\%$ . The yield strength of the  $Zr_{0.5}$  alloy increased to  $1314 \pm 33$  MPa, and the compressive strength reached  $1673 \pm 11$  MPa with no reduction in plastic strain. The  $Zr_1$  alloy yielded at  $1287 \pm 21$  MPa, reaching a maximum strength of  $1518 \pm 16$  MPa and a fracture plastic strain of  $8 \pm 1\%$ . It can be found that a proper Zr content improved the mechanical performance of the alloy while maintaining its plasticity. Compared with the  $Zr_0$  alloy, the yield strength and compressive strength of the  $Zr_{0.5}$  alloy were 18.47% and 18.14% higher, respectively.

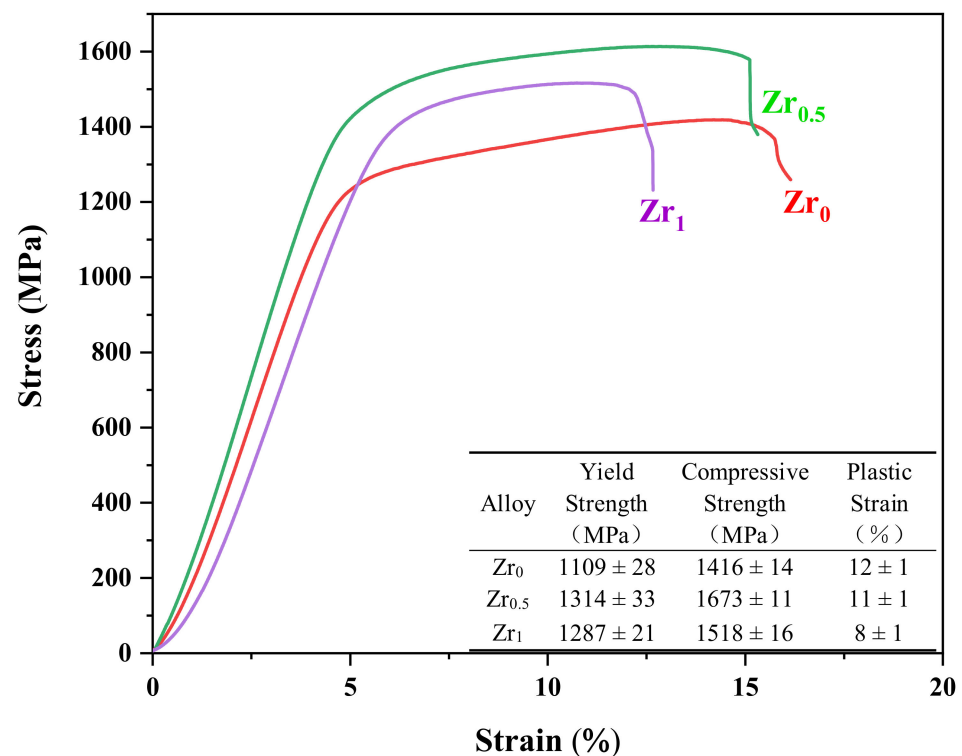


**Figure 3.** Room-temperature compressive stress–strain curves of the  $TiMoNbZr_x$  HEAs. The inset table is the strength and plastic strain of the  $TiMoNbZr_x$  HEAs.

SEM analysis of the cross section of the  $TiMoNbZr_x$  high-entropy alloy was carried out, and the compression fracture morphology is shown in Figure 4. It can be observed from Figure 4a–c that the samples were all broken at  $45^\circ$  without obvious occurrence, indicating that the three alloys have some compressive plasticity. The cleavage steps and complete grain steps can be seen in Figure 4d, indicating that the  $Zr_0$  alloy underwent trans-granular fracture and partial intergranular fracture. After Zr alloying, the number of cracks in the  $Zr_{0.5}$  alloy decreased. Compared with the  $Zr_0$  alloy, the  $Zr_{0.5}$  alloy had more tearing edges (Figure 4e), indicating that it had better ductility and that it changed from ductile and brittle fracture to only ductile fracture. When the Zr content continued to increase, the cleavage steps and cracks increased during the fracture of the  $Zr_1$  alloy (Figure 4f), showing partial transgranular fracture and ductile fracture. The results indicate that the  $Zr_{0.5}$  alloy exhibited the greatest plasticity among the three alloys, which is consistent with

the compression mechanical performance tests. The alloy grain size followed the order of  $Zr_0 > Zr_1 > Zr_{0.5}$ , which is consistent with the microstructure analysis.

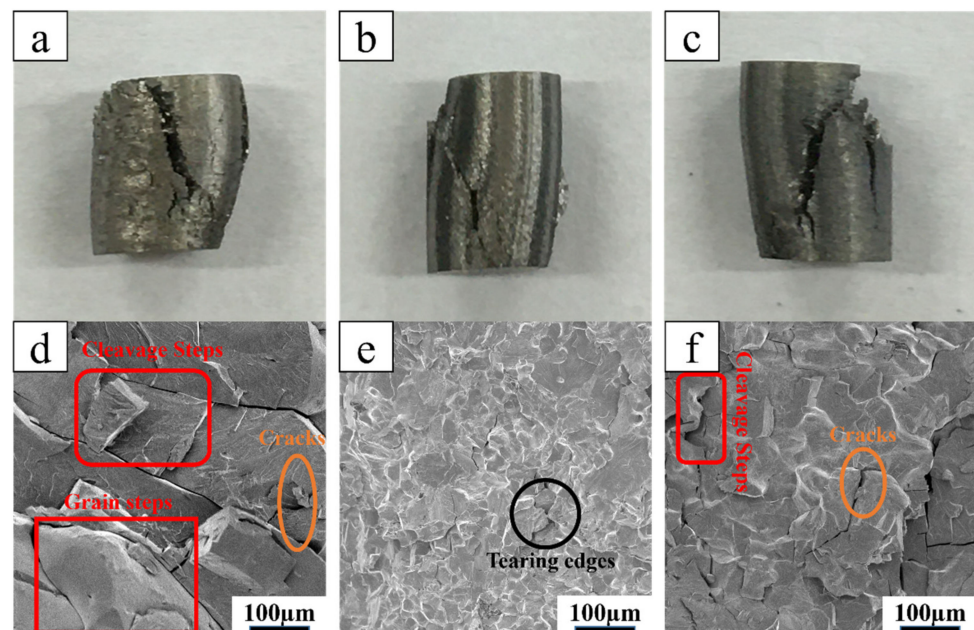


**Figure 4.** Photos and SEM images of the fractured TiMoNbZr<sub>x</sub> HEAs: (a,d) Zr<sub>0</sub>; (b,e) Zr<sub>0.5</sub>; (c,f) Zr<sub>1</sub>.

The hardness of a material is an important indicator of its wear resistance. Before the wear tests, the room-temperature hardness of TiMoNbZr<sub>x</sub> was measured, and the results are shown in Figure 5. The hardness of Zr<sub>0</sub>, Zr<sub>0.5</sub>, and Zr<sub>1</sub> alloys were  $438 \pm 38$ ,  $516 \pm 52$ , and  $489 \pm 43$  HV, respectively. As observed, the hardness of the alloys increased first and then decreased upon increasing the Zr content, and the hardness of the Zr<sub>0.5</sub> alloy was the largest. According to the solid solution strengthening formula [46],

$$\Delta\sigma_s = M \frac{Gc^{\frac{1}{2}}\varepsilon_s^{\frac{3}{2}}}{700} \quad (1)$$

where  $M$  is the Taylor coefficient (2.75 [47]), and  $G$  is the shear modulus of the TiMoNb alloy (68.93 GPa). It can be converted to the shear modulus using Young's modulus ( $E = 183.37$  GPa) and Poisson's ratio ( $\nu = 0.33$ ) as follows [48]:

$$G = \frac{E}{2(1+\nu)} \quad (2)$$

where  $c$  is the concentration of solid solution atoms, and  $\varepsilon_s$  is jointly determined by differences in the moduli and atomic sizes (labeled  $\varepsilon_G$  and  $\varepsilon_a$ ), which can be estimated by

$$\varepsilon_s = \left| \frac{\varepsilon_G}{1+0.5\varepsilon_G} - 3\varepsilon_a \right| \quad (3)$$

In the equation,  $\varepsilon_G$  and  $\varepsilon_a$  are defined as

$$\varepsilon_G = \frac{1}{G} \frac{\partial G}{\partial c}, \quad \varepsilon_a = \frac{1}{a} \frac{\partial a}{\partial c} \quad (4)$$

where  $\varepsilon_G$  is generally negligible, compared to  $\varepsilon_a$ , and  $a$  is the lattice parameter.

$\Delta\sigma_s$  for Zr<sub>0.5</sub> and Zr<sub>1</sub> were calculated to be 4.69 MPa and 6.88 MPa, respectively, which suggests an enhanced strengthening effect upon increasing the Zr atomic percentage, and the Zr<sub>1</sub> solid solution strengthening effect is the greatest. Zr<sub>0.5</sub> had the smallest crystal

grains, with the best grain boundary strengthening effect. Under the combined action of solid solution strengthening and grain boundary strengthening,  $Zr_{0.5}$  displayed the best mechanical performance.

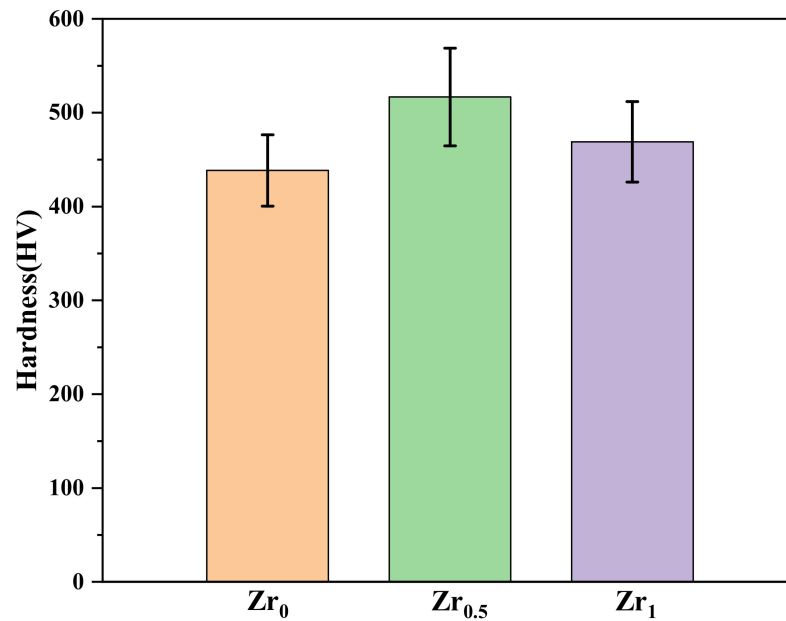


Figure 5. Hardness of the TiMoNbZr<sub>x</sub> HEAs.

### 3.4. Wear Behavior under Friction

Figure 6 shows the relationship between the friction coefficient and wear time of the TiMoNbZr<sub>x</sub> alloys under different loads (30 N, 50 N, and 100 N). At the beginning of friction and wear, the friction coefficient of the alloy increased rapidly. Upon extending the wear time, the friction coefficient gradually stabilized and became smoother as the load increased. At 30 N, 50 N, and 100 N, the average friction coefficients were 0.45, 0.42, and 0.40 for  $Zr_0$  alloy; 0.42, 0.37, and 0.32 for  $Zr_{0.5}$  alloy; and 0.30, 0.32, and 0.34 for  $Zr_1$  alloy.

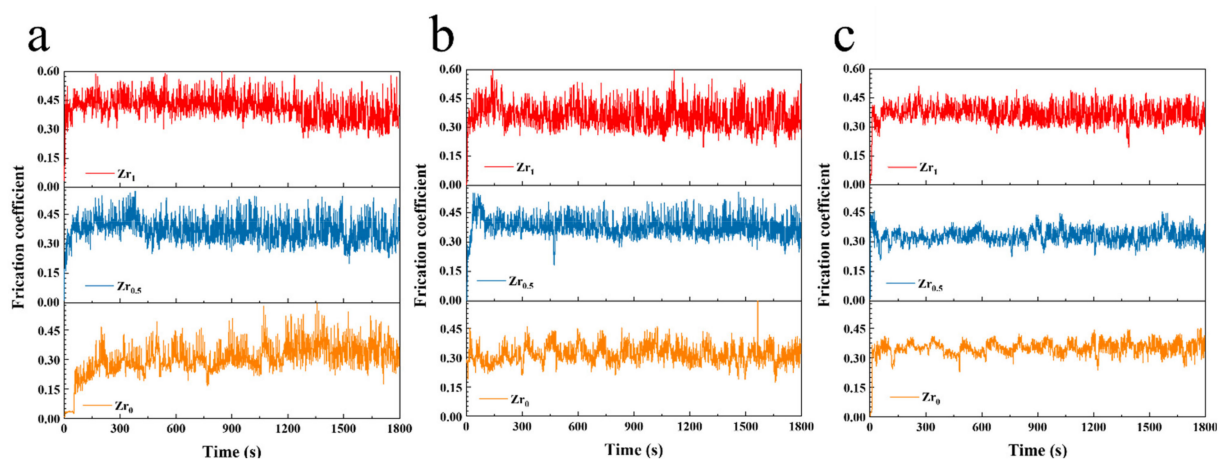


Figure 6. Friction coefficients versus time for the TiMoNbZr<sub>x</sub> HEAs under different loads: (a) 30 N; (b) 50 N; (c) 100 N.

The wear scar morphology of the samples under different loads was characterized by SEM, as shown in Figure 7. The wear scar surface was relatively flat, with different numbers of furrows and white peeling edges, the width of which increased as the load increased. Under the same load, many particles accumulated, and there was unevenness on the surfaces of the  $Zr_0$  and  $Zr_1$  alloy wear scars. The wear scar surface of the  $Zr_{0.5}$

alloy had nearly no accumulated particles, and the whole surface was relatively flat and smooth. The wear scar morphology was further enlarged and analyzed in depth, as shown in Figure 8. Under the same load, the surface of the  $Zr_0$  alloy was broken and a large area peeled off during the wear process. Exfoliation occurred and large cracks and wear particles appeared on the surface (see the black accumulation in Figure 8) (Figure 8a–c). Compared with the  $Zr_0$  alloy, the surface of the  $Zr_{0.5}$  alloy was smooth and flat after wear, and longitudinal cracks disappeared and furrows appeared (Figure 8d–f). Various wear particles appeared on the surface of the  $Zr_1$  alloy, and the surface was relatively flat with a small amount of exfoliation (Figure 8g–i). In addition, under different loads, the wear surface of all three alloys was smooth, longitudinal cracks were reduced, transverse cracks disappeared, and the wear resistance of the alloys increased with the load.

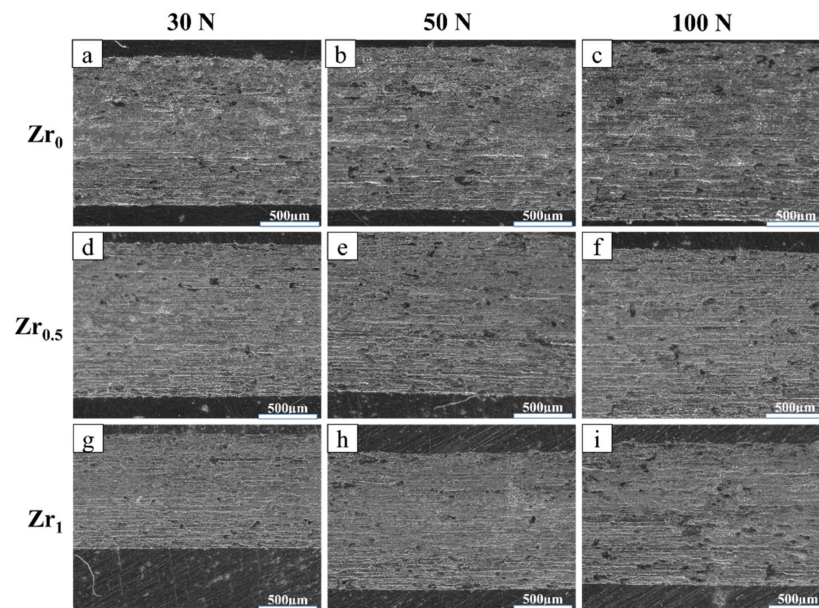


Figure 7. SEM image of the wear tracks of the TiMoNbZr<sub>x</sub> HEAs under loads of 30, 50, and 100 N: (a–c)  $Zr_0$ ; (d–f)  $Zr_{0.5}$ ; (g–i)  $Zr_1$ .

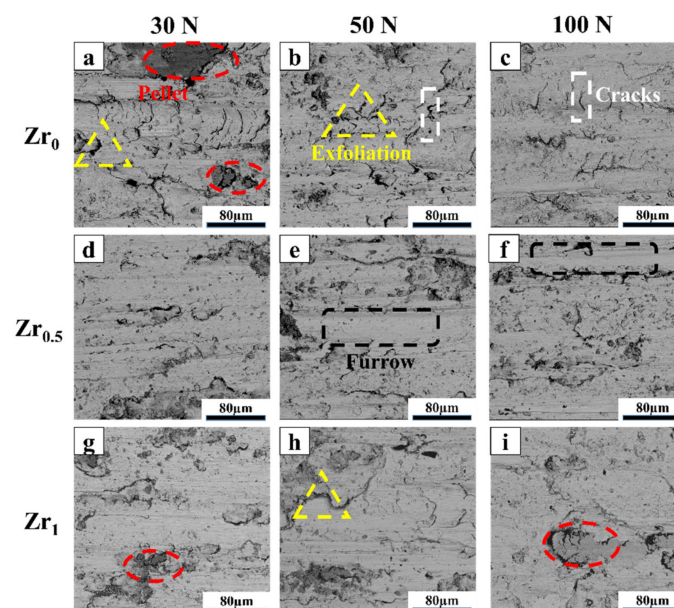
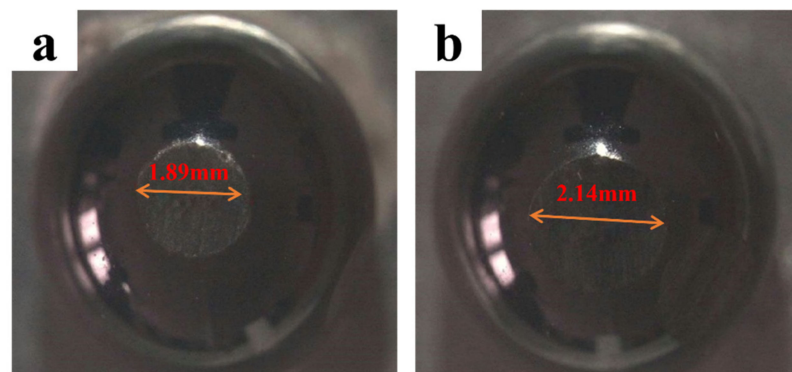
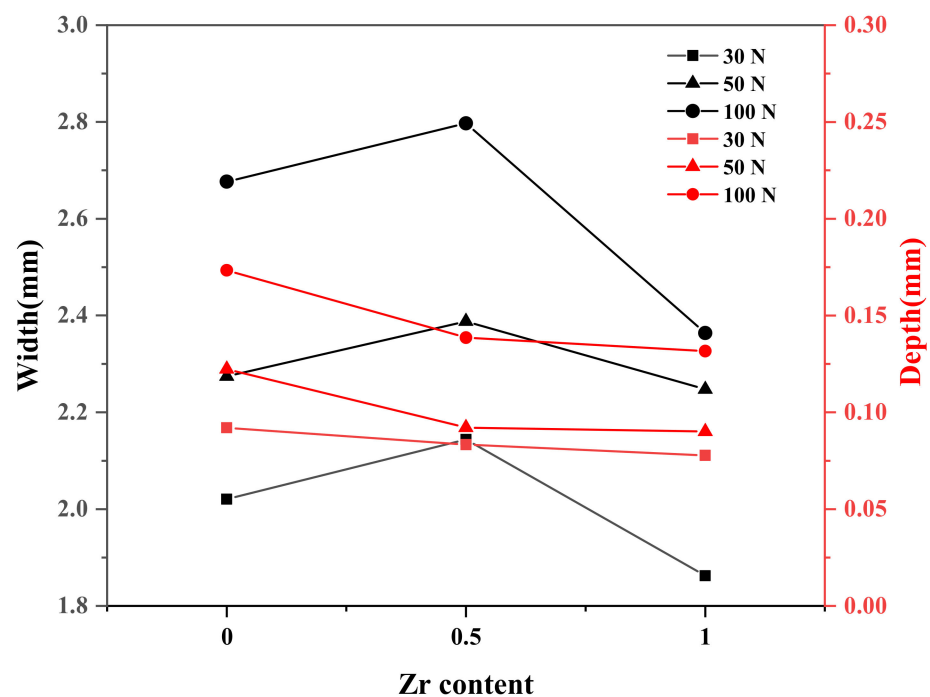


Figure 8. Microstructure of the wear tracks of the TiMoNbZr<sub>x</sub> HEAs under loads of 30, 50, and 100 N: (a–c)  $Zr_0$ ; (d–f)  $Zr_{0.5}$ ; (g–i)  $Zr_1$ .

Furthermore, the wear of the grinding balls under different loads was analyzed, and the optical microscope images are shown in Figure 9. The cross sections of the wear on the alloy grinding ball were all round, at 30 N, 50 N, and 100 N. As for the  $Zr_0$  alloy, the diameters of the grinding ball wear surface were 1.79, 1.89, and 2.33 mm, respectively. As for the  $Zr_{0.5}$  alloy, the diameters of its grinding ball wear surface were 1.82, 2.14, and 2.49 mm, respectively. As for the  $Zr_1$  alloy, the diameters of its grinding ball wear surface were 1.80, 2.11, and 2.17 mm, respectively. According to these results, a proper amount of Zr alloying improved the wear resistance of the  $Zr_0$  alloy, which is consistent with the wear scar analysis. In addition, the width and depth of the sample wear scar were measured by a profiler and plotted in Figure 10. The  $Zr_{0.5}$  alloy had the greatest width under different loads, while the depth was relatively shallow, which once again shows that a proper amount of Zr alloying improved the wear resistance of the  $Zr_0$  alloy.



**Figure 9.** Optical images of  $Si_3N_4$  counter-face used in the wear tests of  $Zr_0$  (a) and  $Zr_{0.5}$  (b) under a 50 N load.



**Figure 10.** Wear width and depth of the  $TiMoNbZr_x$  HEAs under loads of 30, 50, and 100 N.

To explore the reasons for its excellent wear resistance and wear mechanism, the  $Zr_{0.5}$  alloy wear scar morphology under a 100 N load was characterized by SEM, and SEM-EDS (Figure 11). As observed, Ti, Mo, Nb, and Zr elements were concentrated in the smooth and flat area, and N and Si were segregated in the black area. In addition, a large amount of

oxygen was found, whose mole fraction was as high as 20.50%. Due to the nature of Zr, it is easily oxidized and binds to atmospheric oxygen to form large amounts of oxides, which can act as a lubricant that reduces the friction [37] and the wear rate of the  $Zr_{0.5}$  alloy.

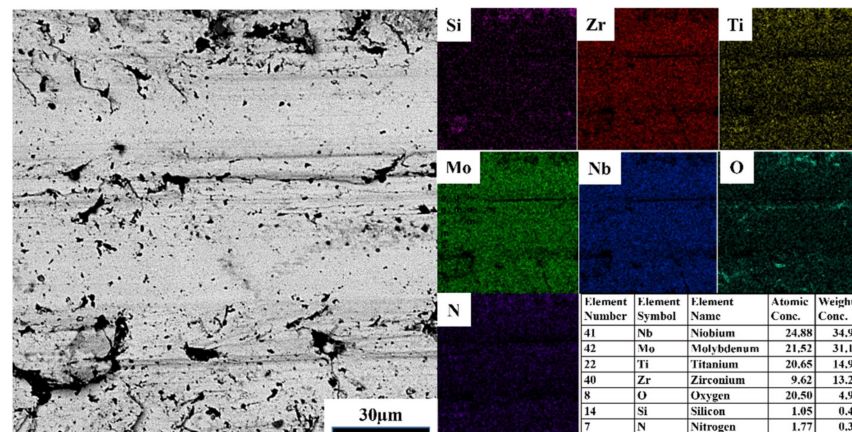


**Figure 11.** Morphology and EDX analysis of the wear tracks of the  $Zr_{0.5}$  under a 100 N load.

#### 4. Conclusions

In this paper, a  $TiMoNbZr_x$  alloy was prepared by arc smelting, and its phase composition, microstructure, mechanical properties, and wear resistance were systematically studied. The following conclusions were drawn:

- (1) The alloys after Zr addition were composed of a single BCC phase. Upon increasing the Zr content, the lattice constant and solid solution strengthening increased. The alloy structure transformed from an equiaxed crystal-dendritic to a crystal-equiaxed crystal morphology, and the alloy grain size first decreased and then increased.
- (2) A proper amount of Zr alloying increased the strength and hardness of the alloy while maintaining its plasticity. Compared with the  $Zr_0$  alloy, the yield strength and compressive strength of the  $Zr_{0.5}$  alloy were increased by 18.47% (to  $1314 \pm 33$  MPa) and 18.14% (to  $1673 \pm 11$  MPa), respectively. Additionally,  $Zr_{0.5}$  exhibited the maximum hardness ( $516 \pm 52$  HV).
- (3)  $Zr_{0.5}$  alloy had the widest wear scar, a relatively low depth, the greatest degree of wear on the grinding ball, and the best wear resistance. These properties were attributed to the generation of an oxide film on the wear surface, which acted as a lubricant.

**Author Contributions:** Conceptualization, G.C. and Y.X.; methodology, X.J., X.L. and Y.T.; formal analysis, Y.H., Z.C. and J.L.; investigation, Y.T., Y.H. and Z.C.; resources, Y.T., Y.H. and X.L.; data curation, Y.X.; writing—original draft preparation, Y.X.; writing—review and editing, Y.X., Y.T., G.C. and X.J. All authors have read and agreed to the published version of the manuscript.

**Funding:** The work was funded by the National Key R&D Program of China, grant number 2018YFC1902401, National Natural Science Foundation of China, grant number 52005053, High-Tech Industry Science and Technology Innovation Leading Program of Hunan Province, grant number 2020GK2085, and Natural Science Foundation of Hunan Province of China, grant number 2019JJ50657 and 2018JJ2426.

**Institutional Review Board Statement:** Not applicable.

**Informed Consent Statement:** Not applicable.

**Data Availability Statement:** The data presented in this study are available on request from the corresponding author.

**Conflicts of Interest:** The authors declare that they have no known competing financial interests or personal relationships that could have appeared to influence the work reported in this paper.

## References

1. Senkov, O.N.; Wilks, G.B.; Miracle, D.B.; Chuang, C.P.; Liaw, P.K. Refractory high-entropy alloys. *Intermetallics* **2010**, *18*, 1758–1765. [[CrossRef](#)]
2. Guo, N.N.; Wang, L.; Luo, L.S.; Li, X.Z.; Chen, R.R.; Su, Y.Q.; Guo, J.J.; Fu, H.Z. Microstructure and mechanical properties of refractory high entropy (Mo 0.5 NbHf 0.5 ZrTi) BCC /M 5 Si 3 in-situ compound. *J. Alloy. Compd.* **2016**, *660*, 197–203. [[CrossRef](#)]
3. Senkov, O.N.; Woodward, C.F. Microstructure and properties of a refractory NbCrMo0.5Ta0.5TiZr alloy. *Mater. Sci. Eng. A* **2011**, *529*, 311–320. [[CrossRef](#)]
4. Wu, Y.D.; Cai, Y.H.; Wang, T.; Si, J.J.; Zhu, J.; Wang, Y.D.; Hui, X.D. A refractory Hf<sub>25</sub>Nb<sub>25</sub>Ti<sub>25</sub>Zr<sub>25</sub> high-entropy alloy with excellent structural stability and tensile properties. *Mater. Lett.* **2014**, *130*, 277–280. [[CrossRef](#)]
5. Couzinié, J.P.; Dirras, G.; Perrière, L.; Chauveau, T.; Leroy, E.; Champion, Y.; Guillot, I. Microstructure of a near-equiatomic refractory high-entropy alloy. *Mater. Lett.* **2014**, *126*, 285–287. [[CrossRef](#)]
6. Xiao, D.H.; Zhou, P.F.; Wu, W.Q.; Diao, H.Y.; Gao, M.C.; Song, M.; Liaw, P.K. Microstructure, mechanical and corrosion behaviors of AlCoCuFeNi-(Cr,Ti) high entropy alloys. *Mater. Des.* **2017**, *116*, 438–447. [[CrossRef](#)]
7. Chang, C.H.; Titus, M.S.; Yeh, J.W. Oxidation Behavior between 700 and 1300 °C of Refractory TiZrNbHfTa High-Entropy Alloys Containing Aluminum. *Adv. Eng. Mater.* **2018**, *20*, 1700948. [[CrossRef](#)]
8. Cao, Y.K.; Liu, Y.; Liu, B.; Zhang, W.D.; Wang, J.W.; Du, M. Effects of Al and Mo on high temperature oxidation behavior of refractory high entropy alloys. *Trans. Nonferrous Met. Soc. China* **2019**, *29*, 1476–1483. [[CrossRef](#)]
9. Gorr, B.; Azim, M.; Christ, H.J.; Mueller, T.; Schliephake, D.; Heilmaier, M. Phase equilibria, microstructure, and high temperature oxidation resistance of novel refractory high-entropy alloys. *J. Alloy. Compd.* **2015**, *624*, 270–278. [[CrossRef](#)]
10. Lu, C.-Y.; Lu, Y.-P. Preface to the special issue on high entropy materials and tungsten-based nuclear materials. *Tungsten* **2021**, *3*, 117–118. [[CrossRef](#)]
11. Wang, X.; Huang, H.; Shi, J.; Xu, H.-Y.; Meng, D.-Q. Recent progress of tungsten-based high-entropy alloys in nuclear fusion. *Tungsten* **2021**, *3*, 143–160. [[CrossRef](#)]
12. Senkov, O.N.; Wilks, G.B.; Scott, J.M.; Miracle, D.B. Mechanical properties of Nb<sub>25</sub>Mo<sub>25</sub>Ta<sub>25</sub>W<sub>25</sub> and V<sub>20</sub>Nb<sub>20</sub>Mo<sub>20</sub>Ta<sub>20</sub>W<sub>20</sub> refractory high entropy alloys. *Intermetallics* **2011**, *19*, 698–706. [[CrossRef](#)]
13. Han, Z.D.; Chen, N.; Zhao, S.F.; Fan, L.W.; Yang, G.N.; Shao, Y.; Yao, K.F. Effect of Ti additions on mechanical properties of NbMoTaW and VNbMoTaW refractory high entropy alloys. *Intermetallics* **2017**, *84*, 153–157. [[CrossRef](#)]
14. Han, Z.D.; Luan, H.W.; Liu, X.; Chen, N.; Li, X.Y.; Shao, Y.; Yao, K.F. Microstructures and mechanical properties of Ti<sub>x</sub>NbMoTaW refractory high-entropy alloys. *Mater. Sci. Eng. A* **2018**, *712*, 380–385. [[CrossRef](#)]
15. Zhang, J.; Hu, Y.; Wei, Q.; Xiao, Y.; Chen, P.; Luo, G.; Shen, Q. Microstructure and mechanical properties of RexNbMoTaW high-entropy alloys prepared by arc melting using metal powders. *J. Alloy. Compd.* **2020**, *827*, 154301. [[CrossRef](#)]
16. Senkov, O.N.; Scott, J.M.; Senkova, S.V.; Meisenkothen, F.; Miracle, D.B.; Woodward, C.F. Microstructure and elevated temperature properties of a refractory TaNbHfZrTi alloy. *J. Mater. Sci.* **2012**, *47*, 4062–4074. [[CrossRef](#)]
17. Senkov, O.N.; Scott, J.M.; Senkova, S.V.; Miracle, D.B.; Woodward, C.F. Microstructure and room temperature properties of a high-entropy TaNbHfZrTi alloy. *J. Alloy. Compd.* **2011**, *509*, 6043–6048. [[CrossRef](#)]
18. Lin, C.-M.; Juan, C.-C.; Chang, C.-H.; Tsai, C.-W.; Yeh, J.-W. Effect of Al addition on mechanical properties and microstructure of refractory AlxHfNbTaTiZr alloys. *J. Alloy. Compd.* **2015**, *624*, 100–107. [[CrossRef](#)]
19. Juan, C.-C.; Tseng, K.-K.; Hsu, W.-L.; Tsai, M.-H.; Tsai, C.-W.; Lin, C.-M.; Chen, S.-K.; Lin, S.-J.; Yeh, J.-W. Solution strengthening of ductile refractory HfMo<sub>x</sub>NbTaTiZr high-entropy alloys. *Mater. Lett.* **2016**, *175*, 284–287. [[CrossRef](#)]
20. Zhang, B.; Gao, M.C.; Zhang, Y.; Guo, S.M. Binary refractory high-entropy alloy Cr MoNbTaVW. *Calphad* **2015**, *51*, 193–201. [[CrossRef](#)]
21. Fernández-Caballero, A.; Wróbel, J.S.; Mummery, P.M.; Nguyen-Manh, D. Short-Range Order in High Entropy Alloys: Theoretical Formulation and Application to Mo-Nb-Ta-V-W System. *J. Phase Equilibria Diffus.* **2017**, *38*, 391–403. [[CrossRef](#)]
22. Kang, B.; Lee, J.; Ryu, H.J.; Hong, S.H. Ultra-high strength WNbMoTaV high-entropy alloys with fine grain structure fabricated by powder metallurgical process. *Mater. Sci. Eng. A* **2018**, *712*, 616–624. [[CrossRef](#)]
23. Senkov, O.N.; Senkova, S.V.; Miracle, D.B.; Woodward, C. Mechanical properties of low-density, refractory multi-principal element alloys of the Cr–Nb–Ti–V–Zr system. *Mater. Sci. Eng. A* **2013**, *565*, 51–62. [[CrossRef](#)]
24. Tian, F.; Varga, L.K.; Chen, N.; Shen, J.; Vitos, L. Ab initio design of elastically isotropic TiZrNbMoV high-entropy alloys. *J. Alloy. Compd.* **2014**, *599*, 19–25. [[CrossRef](#)]
25. Butler, T.M.; Chaput, K.J.; Dietrich, J.R.; Senkov, O.N. High temperature oxidation behaviors of equimolar NbTiZrV and NbTiZrCr refractory complex concentrated alloys (RCCAs). *J. Alloy. Compd.* **2017**, *729*, 1004–1019. [[CrossRef](#)]
26. Tian, L.-Y.; Wang, G.; Harris, J.S.; Irving, D.L.; Zhao, J.; Vitos, L. Alloying effect on the elastic properties of refractory high-entropy alloys. *Mater. Des.* **2017**, *114*, 243–252. [[CrossRef](#)]
27. Jensen, J.K.; Welk, B.A.; Williams, R.E.A.; Sosa, J.M.; Huber, D.E.; Senkov, O.N.; Viswanathan, G.B.; Fraser, H.L. Characterization of the microstructure of the compositionally complex alloy Al<sub>1</sub>Mo<sub>0.5</sub>Nb<sub>1</sub>Ta<sub>0.5</sub>Ti<sub>1</sub>Zr<sub>1</sub>. *Scr. Mater.* **2016**, *121*, 1–4. [[CrossRef](#)]
28. Melia, M.A.; Whetten, S.R.; Puckett, R.; Jones, M.; Heiden, M.J.; Argibay, N.; Kustas, A.B. High-throughput additive manufacturing and characterization of refractory high entropy alloys. *Appl. Mater. Today* **2020**, *19*, 100560. [[CrossRef](#)]
29. Senkov, O.N.; Jensen, J.K.; Pilchak, A.L.; Miracle, D.B.; Fraser, H.L. Compositional variation effects on the microstructure and properties of a refractory high-entropy superalloy AlMo<sub>0.5</sub>NbTa<sub>0.5</sub>TiZr. *Mater. Des.* **2018**, *139*, 498–511. [[CrossRef](#)]

30. Senkov, O.N.; Kuhr, S.J.; Shank, J.M.; Payton, E.J.; Woodward, C. Microstructure and properties of an equiatomic TaTiZr alloy. *Mater. Sci. Eng. A* **2021**, *814*, 141168. [[CrossRef](#)]
31. Senkov, O.N.; Gild, J.; Butler, T.M. Microstructure, mechanical properties and oxidation behavior of NbTaTi and NbTaZr refractory alloys. *J. Alloy. Compd.* **2021**, *862*, 158003. [[CrossRef](#)]
32. Yurchenko, N.; Panina, E.; Zherebtsov, S.; Stepanov, N. Design and characterization of eutectic refractory high entropy alloys. *Materialia* **2021**, *16*, 101057. [[CrossRef](#)]
33. Yurchenko, N.; Panina, E.; Tikhonovsky, M.; Salishchev, G.; Zherebtsov, S.; Stepanov, N. Structure and mechanical properties of an in situ refractory Al<sub>20</sub>Cr<sub>10</sub>Nb<sub>15</sub>Ti<sub>20</sub>V<sub>25</sub>Zr<sub>10</sub> high entropy alloy composite. *Mater. Lett.* **2020**, *264*, 127372. [[CrossRef](#)]
34. Wei, S.; Kim, S.J.; Kang, J.; Zhang, Y.; Zhang, Y.; Furuhashi, T.; Park, E.S.; Tasan, C.C. Natural-mixing guided design of refractory high-entropy alloys with as-cast tensile ductility. *Nat. Mater.* **2020**, *19*, 1175–1181. [[CrossRef](#)]
35. Jia, Y.-J.; Chen, H.-N.; Liang, X.-D. Microstructure and wear resistance of CoCrNbNiW high-entropy alloy coating prepared by laser melting deposition. *Rare Met.* **2019**, *38*, 1153–1159. [[CrossRef](#)]
36. Pouliou, A.; Georgatis, E.; Lekatou, A.; Karantzalis, A.E. Microstructure and wear behavior of a refractory high entropy alloy. *Int. J. Refract. Met. Hard Mater.* **2016**, *57*, 50–63. [[CrossRef](#)]
37. Mathiou, C.; Pouliou, A.; Georgatis, E.; Karantzalis, A.E. Microstructural features and dry-sliding wear response of MoTaNbZrTi high entropy alloy. *Mater. Chem. Phys.* **2018**, *210*, 126–135. [[CrossRef](#)]
38. Zhu, W.; Zhao, C.; Zhang, Y.; Kwok, C.T.; Luan, J.; Jiao, Z.; Ren, F. Achieving exceptional wear resistance in a compositionally complex alloy via tuning the interfacial structure and chemistry. *Acta Mater.* **2020**, *188*, 697–710. [[CrossRef](#)]
39. Zeng, Q.; Xu, Y. A comparative study on the tribocorrosion behaviors of AlFeCrNiMo high entropy alloy coatings and 304 stainless steel. *Mater. Today Commun.* **2020**, *24*, 101261. [[CrossRef](#)]
40. Tong, Y.; Bai, L.; Liang, X.; Chen, Y.; Zhang, Z.; Liu, J.; Li, Y.; Hu, Y. Influence of alloying elements on mechanical and electronic properties of NbMoTaWX (X = Cr, Zr, V, Hf and Re) refractory high entropy alloys. *Intermetallics* **2020**, *126*, 106928. [[CrossRef](#)]
41. Jiang, H.; Jiang, L.; Lu, Y.P.; Wang, T.M.; Cao, Z.Q.; Li, T.J. Microstructure and Mechanical Properties of the W-Ni-Co System Refractory High-Entropy Alloys. *MSF* **2015**, *816*, 324–329. [[CrossRef](#)]
42. Yurchenko, N.Y.; Stepanov, N.D.; Gridneva, A.O.; Mishunin, M.V.; Salishchev, G.A.; Zherebtsov, S.V. Effect of Cr and Zr on phase stability of refractory Al-Cr-Nb-Ti-V-Zr high-entropy alloys. *J. Alloy. Compd.* **2018**, *757*, 403–414. [[CrossRef](#)]
43. Qiao, D.X.; Jiang, H.; Jiao, W.N.; Lu, Y.P.; Cao, Z.Q.; Li, T.J. A Novel Series of Refractory High-Entropy Alloys Ti<sub>2</sub>ZrHf<sub>0.5</sub>VNb<sub>x</sub> with High Specific Yield Strength and Good Ductility. *Acta Metall. Sin.* **2019**, *32*, 925–931. [[CrossRef](#)]
44. Zhang, M.; Zhou, X.; Zhu, W.; Li, J. Influence of Annealing on Microstructure and Mechanical Properties of Refractory CoCr-MoNbTi<sub>0.4</sub> High-Entropy Alloy. *Metall. Mater. Trans. A* **2018**, *49*, 1313–1327. [[CrossRef](#)]
45. Li, X.; Tian, F.; Schönecker, S.; Zhao, J.; Vitos, L. Ab initio-predicted micro-mechanical performance of refractory high-entropy alloys. *Sci. Rep.* **2015**, *5*, 12334. [[CrossRef](#)] [[PubMed](#)]
46. He, J.Y.; Wang, H.; Huang, H.L.; Xu, X.D.; Chen, M.W.; Wu, Y.; Liu, X.J.; Nieh, T.G.; An, K.; Lu, Z.P. A precipitation-hardened high-entropy alloy with outstanding tensile properties. *Acta Mater.* **2016**, *102*, 187–196. [[CrossRef](#)]
47. Rao, S.I.; Woodward, C.; Akdim, B.; Senkov, O.N.; Miracle, D. Theory of solid solution strengthening of BCC Chemically Complex Alloys. *Acta Mater.* **2021**, *209*, 116758. [[CrossRef](#)]
48. Xu, S.; Hwang, E.; Jian, W.-R.; Su, Y.; Beyerlein, I.J. Atomistic calculations of the generalized stacking fault energies in two refractory multi-principal element alloys. *Intermetallics* **2020**, *124*, 106844. [[CrossRef](#)]